Simultaneous Measurement of Cathode Surface Temperature Distribution and Plasma Spatial Distribution in Self-Field MPD Thruster

IEPC-2019-551

Presented at the 36th International Electric Propulsion Conference
University of Vienna • Vienna, Austria
September 15-20, 2019

Shitan Tauchi[1]
SOKENDAI (The Graduate University for Advanced Studies), Sagamihara, Kanagawa, 252-5210, Japan

Yuya Oshio[2]
Ryukoku University, Otsu, Shiga, 520-2194, Japan

Akira Kawasaki[3]
Nagoya University, Nagoya, Aichi, 464-8603, Japan

and

Ikkoh Funaki[4]
Japan Aerospace Exploration Agency, Sagamihara, Kanagawa, 252-5210, Japan

Abstract: The cathode surface temperature and plasma flow field in the discharge chamber were measured simultaneously to clarify the relationships between cathode surface temperature distribution and plasma spatial distribution at the near cathode region of a self-field magnetoplasmadynamic (SF-MPD) thruster. The thruster was operated at discharge currents both 9 kA and 13 kA for hydrogen and argon propellants, and mass flow rate of 0.3 g/s and 0.4 g/s in case of hydrogen propellant, and mass flow rate of 0.7 g/s and 1.89 g/s in case of argon propellant. As a result, we clarify that the electron number density distribution has an effect on the cathode surface temperature distribution, and the electron temperature distribution has an effect on the value of the cathode temperature. In case of hydrogen propellant and mass flow rate of 0.4 g/s, the high electron number density region, and high electron temperature distribution occurs at the cathode tip region, and the cathode was heated significantly. The cathode surface temperature is also expanding from cathode tip to cathode root.

Nomenclature

A	=	calibration coefficient
A_1, A_2	=	coefficient = 4, 3.28
C_b	=	coefficient = 0.0143888
c_0	=	speed of light, m/s
e	=	elementary charge

[1] Ph. D. student, Department of Space and Astronautical Science, s.tauchi@ac.jaxa.jp.
[2] Assistant Professor, Department of Mechanical and Systems, oshio@rins.ryukoku.ac.jp.
[3] Assistant Professor, Department of Aerospace Engineering, kawasaki@nuae.nagoya-u.ac.jp.
[4] Professor, Institute of Space and Astronautical Science, funaki.ikkoh@jaxa.jp.

h	=	Planck's constant
I_1, I_2	=	brightness
I	=	current
J	=	discharge current, kA
k	=	Boltzmann constant
$\dot{m}$	=	mass flow rate, g/s
N	=	number density, m^{-3}
r	=	radius, mm
T	=	temperature, K
V	=	discharge voltage, V
V_d	=	bias voltage
V_f	=	floating potential
V_p	=	space potential
$\varepsilon_1, \varepsilon_2$	=	emissivity
λ_1, λ_2	=	wavelength
Subscript		
a	=	anode
c	=	cathode
e	=	electron
i	=	ion
p	=	probe

I. Introduction

IN recent years, various kinds of deep space missions are actively studied.[1,2] The international space exploration coordination group (ISECG) plans the manned Mars mission in the next three decades.[3] The high power electric propulsion is one of the candidates to achieve those missions because of their high specific impulse and high ΔV.[4–7] A magnetoplasmadynamic (MPD) thruster has been a promising candidate as a main thruster for a future deep-space probe owing to its high specific impulse and high thrust density per a thruster head.[8] This study deals with self-field type MPD thruster, which consists of a central cathode and coaxial anode that surrounds the cathode as shown in Fig. 1. The propellant, which flows from upstream to downstream, is heated and ionized by high arc discharge between anode and cathode in the discharge chamber. The Lorentz force (electromagnetic thrust) and gas-dynamic thrust are the main thrust in the thruster. The Lorentz force generated by the interaction between the current flowing from anode to cathode and the self-induced magnetic field.

In the actual mission, the MPD thruster requires input power of over 1 MW, thrust efficiency of over 60 %, specific impulse of about 4000 s, and the lifetime of 1 to 3 years.[9] Although many studies have been conducted for the improvement of thruster performance, these studies have not considered the thermal durability.[10–12] The cathode erosion goes hand in hand with thermal durability in the thruster. Therefore, no devices are accomplished for these requirements.

We have worked on research on self-field MPD thrusters for MW-class in-space propulsion by experiment and numerical means. The ultimate goal of our research is to obtain the design guideline of the thruster, which has high

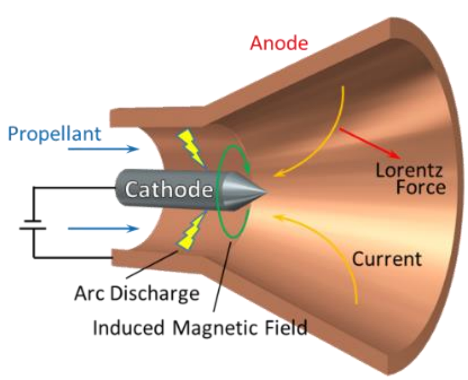

Fig. 1 Operation principle of a self-field MPD thruster.

thruster performance (thrust of 100 N class, thrust efficiency of over 60% (over Hall effect thruster), a specific impulse of 4000 s), and the high thermal durability. To accomplish this goal, we have been performed both numerical simulation, which is thermal analysis and MHD coupled analysis, and experiment. In order to the improvement of cathode thermal durability, a proper understanding of the cathode thermal characteristics is required. In the previous experimental works, the two-color thermography was developed and the cathode surface temperature distribution measurement was conducted by using the two-color thermography in order to proper understanding of the cathode thermal characteristics.[13,14] According to the previous study, the cathode was heated locally on the cathode surface. In particular, the cathode was significantly heated on the cathode tip.[14] The MPD thruster discharge was maintained by the thermionic electrons. Therefore, it is considered that the cathode heating area has an effect on the plasma-flow-field in the thruster, especially near cathode region. However, there is no experimental evidence for the relationships between cathode surface temperature and plasma-flow-field because of no previous study for simultaneous measurement of cathode surface temperature and plasma spatial distribution on the thruster. Therefore, we need to measure the cathode surface temperature and plasma spatial distribution in order to obtain the experimental evidence for the interaction between cathode surface temperature distribution and plasma spatial distribution.

In this study, simultaneous measurement of cathode surface temperature distribution and plasma spatial distribution in the discharge chamber was conducted to clarify the relationship between the cathode surface temperature and the near cathode region plasmas.

II. Experimental Apparatus

A. Facility and MPD Thruster

The experiment was performed in a 2 m in diameter × 3 m long stainless vacuum chamber at the Institute of Space and Astronautical Science (ISAS), JAXA. The vacuum chamber was vacuumed by using a rotary pump, a mechanical booster pump, a turbo molecular pump, and a cryogenic pump, and reach to the vacuum degree in about 7×10^{-5} Pa.

The MPD thruster, MK-2 thruster, was developed by numerical simulation code (MAPS) to satisfy compatibility both high thrust performance and high thermal durability.[15,16] The thruster consists of a copper straight anode and a

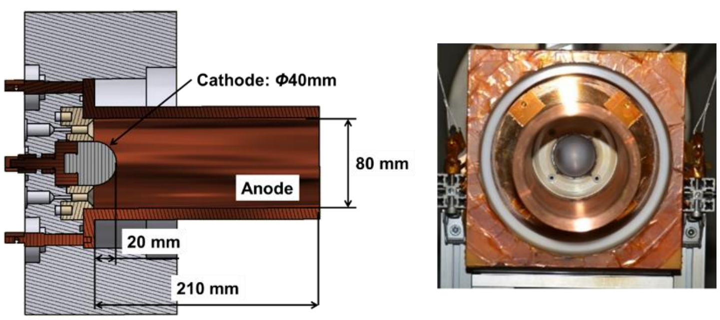

Fig. 2 MK-2 thruster configuration parameters.

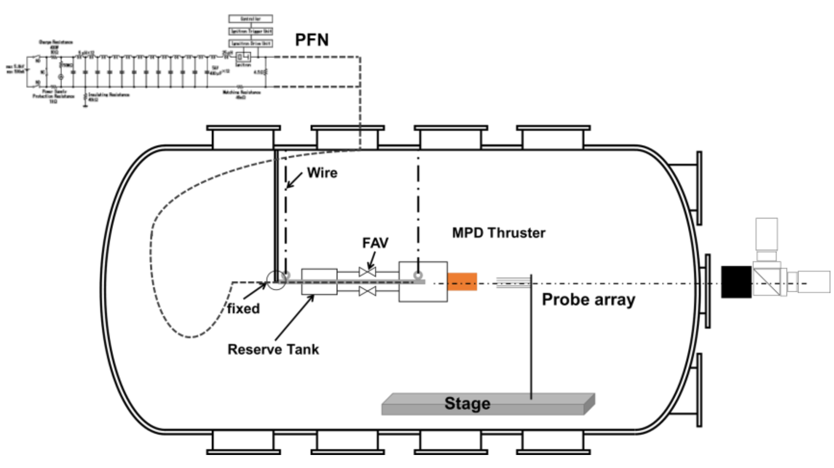

Fig. 3 Experimental setup.

W-2%La_2O_3 rod cathode. Figure 2 shows the thruster configuration parameters. The boron nitride backplate insulator is put between electrodes. The thruster was installed on the pendulum type thrust stand, which is tied up with the vacuum chamber as shown in Fig. 3. The experiments in this study were conducted on the quasi-steady-state operation by using the capacitor bank and the pulse forming network (PFN). The capacitor bank and the PFN consist of the 12 capacitors of 400 μF and 12 inductors of 5 μH and can supply flat-topped waveform of 1.2 ms and discharge current of up to 25 kA. The U_RD CTL-30-S220-4L Rogowski coil was used to measure the discharge current, and the discharge voltage was measured by using a YOKOGAWA 701930 clamp-on current probe via shunt circuit. The four fast-acting valves were used to supply the argon and hydrogen gas as a propellant, and connected with 4 supplying ports. The operation sequence was controlled by using the pulse delay generator.

B. Two-Color Thermography

We developed the two-color thermography to measure the two-dimensional image of cathode surface temperature distribution through MPD arc discharge plasma.[13,14,17] A black body radiates a continuous spectrum dependence on the temperature. The two-color thermography can measure the brightness of each two wavelengths in the same continuous spectrum from a cathode.

The temperature was calculated from Planck's low as shown in Eq. (1).

$$I = \frac{2hc_0^{\,2}}{\lambda^5} \frac{1}{e^{hc/\lambda kT} - 1} \tag{1}$$

The brightness ratio of Planck's law for each wavelength is given by:

$$\frac{I_1}{I_2} = \frac{\varepsilon_2}{\varepsilon_1} \left(\frac{\lambda_2}{\lambda_1} \right)^5 \frac{1 - \exp\left(\frac{C_b}{\lambda_2 T} \right)}{1 - \exp\left(\frac{C_b}{\lambda_1 T} \right)} \tag{2}$$

where ε_1 and ε_2 have assumed to same values in case of two wavelengths are close, and the Eq. (2) can be modified as Eq. (3).

$$\frac{I_1}{I_2} = \left(\frac{\lambda_2}{\lambda_1} \right)^5 \frac{1 - \exp\left(\frac{C_b}{\lambda_2 T} \right)}{1 - \exp\left(\frac{C_b}{\lambda_1 T} \right)} \tag{3}$$

Equation (3) for the temperature T was solved by using Newton's method. The first derivatives were discretized with the central-difference scheme.

The two-color thermography consists of an smc PENTAX-FA645 120 mm F4 camera lens, a beam splitter, two band path filters, and two CCD cameras. The two near-infrared (NIR) region band path filters were selected for measuring wavelengths, because the peak of the continuous spectrum of cathode radiation exists at the NIR region, and it can attain the high signal-to-noise ratio. The previous study[18] showed that the cathode tip temperature reached to about 3000 K, and the peak of the continuous spectrum of 3000 K black body radiation is between 900 nm to 1000 nm. In addition, the band path filters of the NIR region can reduce the MPD arc plasma wavelength (ultraviolet region). The camera lens focuses the radiation from the cathode, and the radiation was separated by a beam splitter. The two-dimensional brightness distributions of the separated radiations were taken the images by CCD cameras. These images need image registration because of the misalignment of the optical system. The image registration was conducted on intensity-based image registration by using the MATLAB image processing toolbox. The brightness ratio distribution was calculated by these positioning images, and the cathode surface temperature distribution was calculated from Eq. (4), which makes considerate the calibrate coefficient A in Eq. (3), by using Newton's method for each cell.

$$A\frac{I_1}{I_2} = \left(\frac{\lambda_2}{\lambda_1} \right)^5 \frac{1 - \exp\left(\frac{C_b}{\lambda_2 T} \right)}{1 - \exp\left(\frac{C_b}{\lambda_1 T} \right)} \tag{4}$$

The calibration is required for the measurement as shown Eq. (4), because the radiation from the cathode is decayed by the lens and other optical systems. In addition, the difference detection ranges between CCD cameras might be expected on this measurement. Therefore, the measurement needs to the calibration. The calibration was carried out by using a calibrated standard light source (USHIO INC. JPD100V500WCS halogen lamp: certificated by Japan Calibration Service System). The two-color thermography was installed on the outside of the vacuum chamber, and measured from the frontal direction.

C. Double Langmuir Probe

1. *Theory and Analysis*

The double Langmuir probe is one of the methods for plasma diagnostics technic and has often used for the plasma measurement of the plasma thruster, which has no referential potential or high input power. In many MPD thruster studies used the double Langmuir probe for plasma measurement for plume and inner thruster plasma measurement.[19–21] The double Langmuir probe consists of two electrodes, and the bias voltage is applied between two electrodes. Figure 4 shows the typical double Langmuir probe electrical circuit. Therefore, the double Langmuir probe does not need to refer to the ground potential.[22] The voltage to current (VI) characteristics is obtained when the double Langmuir probe insert to the plasmas and applied the bias voltage to between the probe electrodes as shown in Fig. 5. The double Langmuir probe can obtain the electron temperature and electron number density from Eqs. (5) and (6).

- Electron temperature

$$\frac{kT_e}{e} = -\frac{\sum I_i}{A_1\left(\frac{d\,I_p}{d\,V_d}\right)_{V_d=0} - A_2\left(\frac{d\,I_p}{d\,V_d}\right)_{ion\ saturation}} \tag{5}$$

where $(d\,I_p/d\,V_p)_{Vd=0}$ represents slope for the flexion point of VI characteristic, and $(d\,I_p/d\,V_p)_{ion\ saturation}$ indicates the slope for the ion saturation region as shown in Fig 4. In the case of non-collisional plasma, where A_1 and A_2 are 4 and 3.28 respectively. The slope for the ion saturation region was fitted by linear function using the least-square method, and the slope for the electron retarding region was also fitted by linear function using least-square method.

- Electron number density

$$I_{ion\ saturation} = \kappa N_e S\sqrt{\frac{kT_e}{m_i}} \tag{6}$$

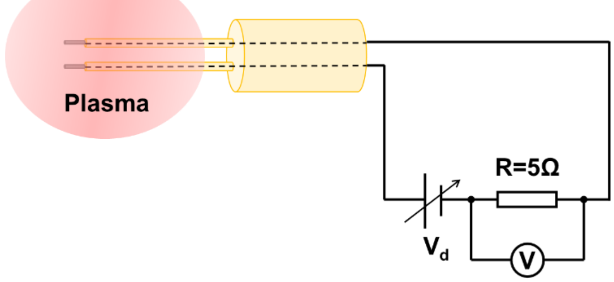

Fig. 4. The electrical circuit for a double Langmuir probe (The shunt circuit resistance sets 5 Ω in this study).

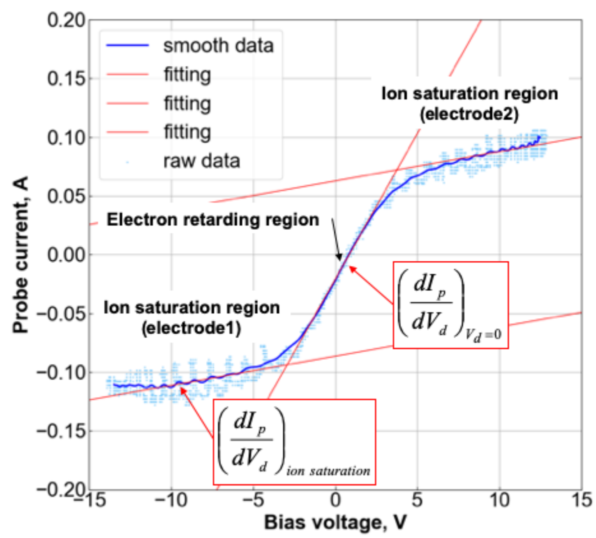

Fig. 5 Typical double Langmuir probe VI characteristic (Ar, 0.7 g/s, 9 kA, z = 265 mm, r = 0 mm).

2. *Probe Design*

In this study, the double Langmuir probe measurement was conducted for the entire region of inner and outer thruster in order to clarify the plasma flow-field of the thruster, especially electron number density, electron temperature, and plasma space potential. The double Langmuir probe consists of two floating electrodes. The probe

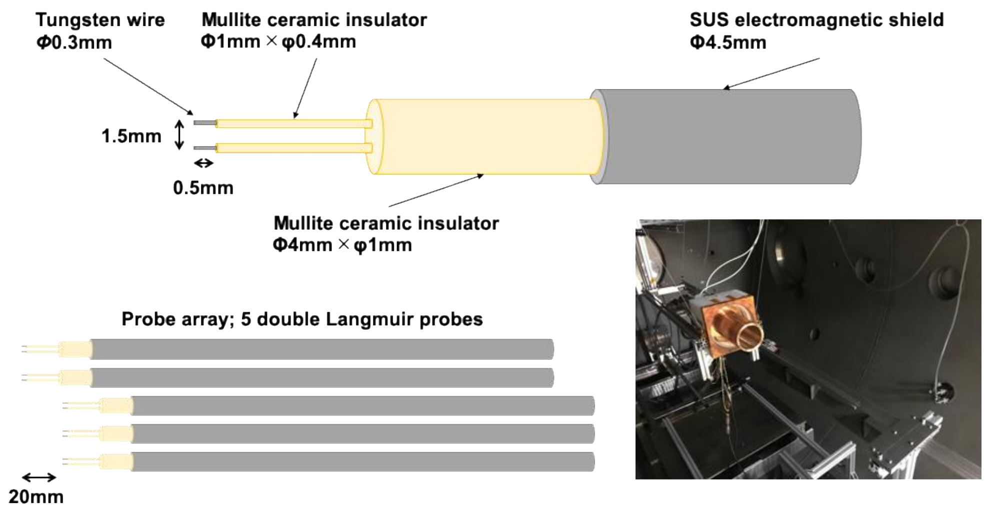

Fig. 6 Double Langmuir probe design.

was designed as shown in Fig. 6. As shown in Fig. 6, the probe consists of two ϕ0.3 mm × 0.5 mm long tungsten wires, ceramic insulator, and the stainless-steel pipe as the electromagnetic shield. The sine curve probe voltage was generated by the NF WF1948 function generator and applied by using the five high-speed bi-polar power supply. The probe was swept from 0.5 ms to 1 ms in MPD discharge as shown in Fig. 7. In this measurement, the five probes were installed on the probe array and swept at the same time.

3. Floating Potential and Space Potential Measurements

The floating potential and space potential measurements were also conducted only in case of hydrogen propellant, mass flow rate of 0.3 g/s, and discharge current of 9 kA. The floating potential was measured by using the voltage probe between one of the double Langmuir probe electrode and the cathode electrode. The space potential was calculated by Eq. (7).

- Space potential

$$V_p = V_f - \frac{kT_e}{e} \ln\left(\frac{\pi M_e}{2M_i}\right)^{1/2} \tag{7}$$

D. Experimental Conditions

Table 1 shows the experimental condition in this study. Figure 6 shows the measurement points of the double probe. The double Langmuir probe measurements were conducted for 0.5 ms to 1 ms discharge and measured three times each measurement locations as shown in Fig. 8, and averaged the three measurement results and mapping to the contour plot as shown in Figs. 10 and 11.

Table. 1 Experimental Condition.

Propellant	Hydrogen, Argon	
Mass flow rate, g/s	Ar	0.7, 1.89
	H_2	0.3, 0.4
Discharge current, kA	9, 13	
Band path filter, nm	Ar	950, 990
	H_2	980, 990
Backpressure, Pa	7×10^{-5}	

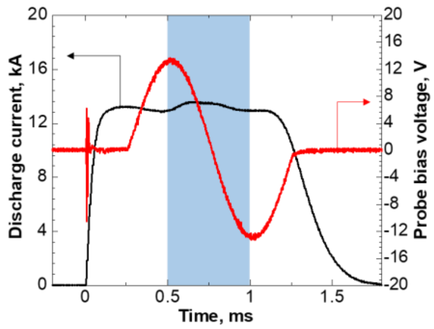

Fig. 7 Probe sweeping area (0.5 ms – 1 ms).

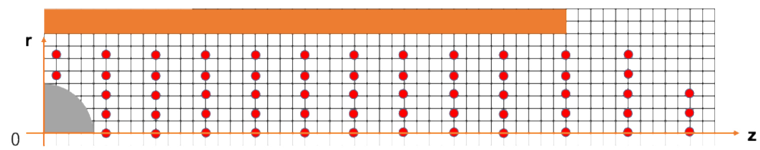

Fig. 8 Measurement point of double probe.

III. Experimental Results and Discussions

A. Cathode Surface Temperature Distribution

This section shows the cathode surface temperature distributions with cases of argon and hydrogen as the propellants. Figure 8 shows the cathode surface temperature distributions in each case. In case of hydrogen propellant and mass flow rate of 0.3 g/s, the images of cathode surface temperature distributions were referred from Ref. 17.

As shown in Fig. 9, the cathode mainly heated both cathode tip and root in case of argon as a propellant. In particular, the cathode root was significantly heated with a discharge current of 9 kA and 13 kA, and the temperature at the cathode root reached to approximately 2800 K. In case of hydrogen as a propellant, the cathode was mainly heated on the cathode tip, and the temperature reached to about 3000 K. The cathode temperature increased with rising the discharge current. The cathode heated area tends to be expanded with increasing the mass flow rate as shown in Fig. 9.

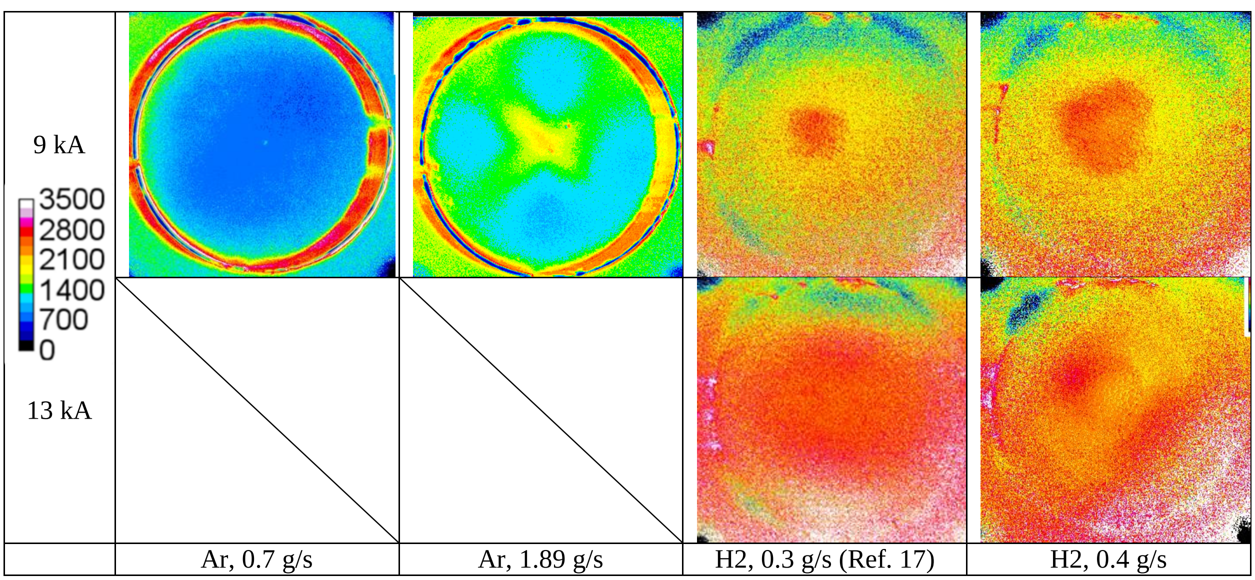

Fig. 9 Cathode surface temperature distributions [K].

B. Plasma Spatial Distribution

This section shows the electron number density, electron temperature, floating potential, and space potential distributions. The floating potential and space potential distributions were only shown in case of hydrogen propellant, the mass flow rate of 0.3 g/s, discharge current of 9 kA. Figure 10 shows the electron number density distributions,

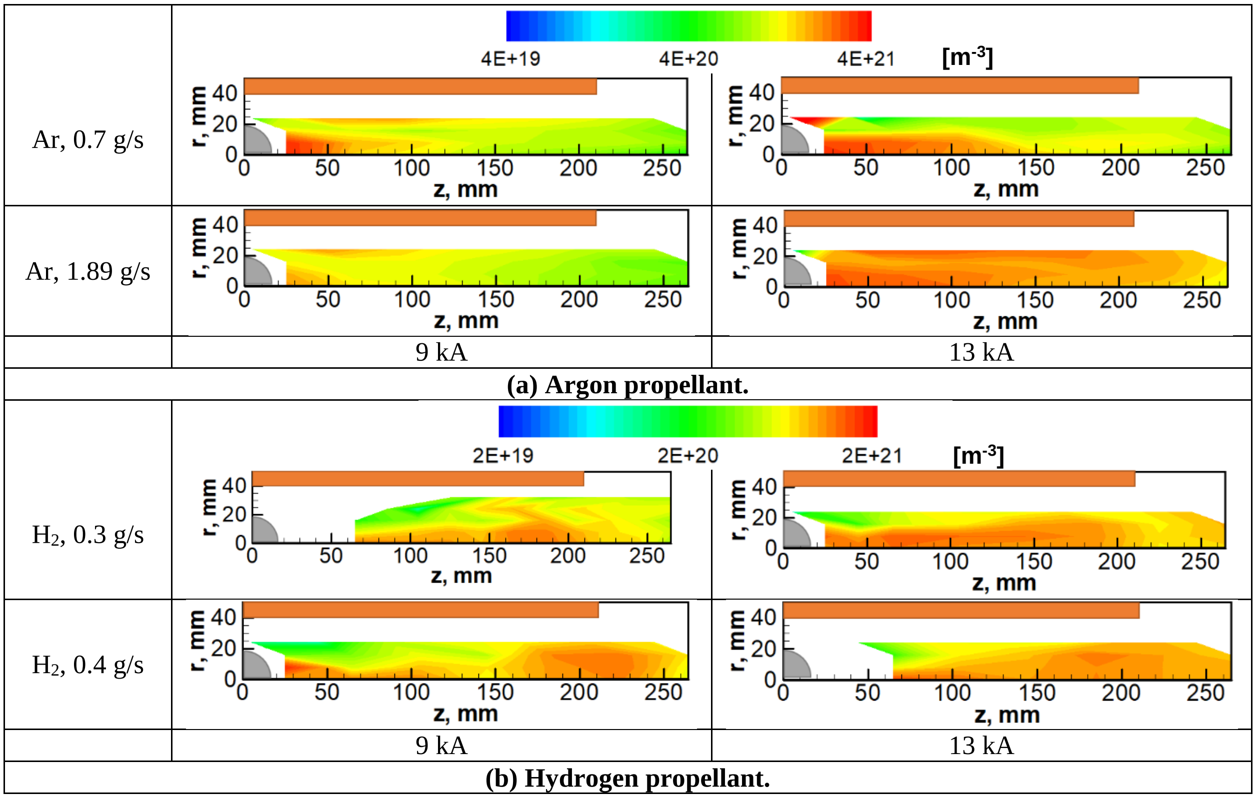

Fig. 10 Electron number density distributions [m^{-3}].

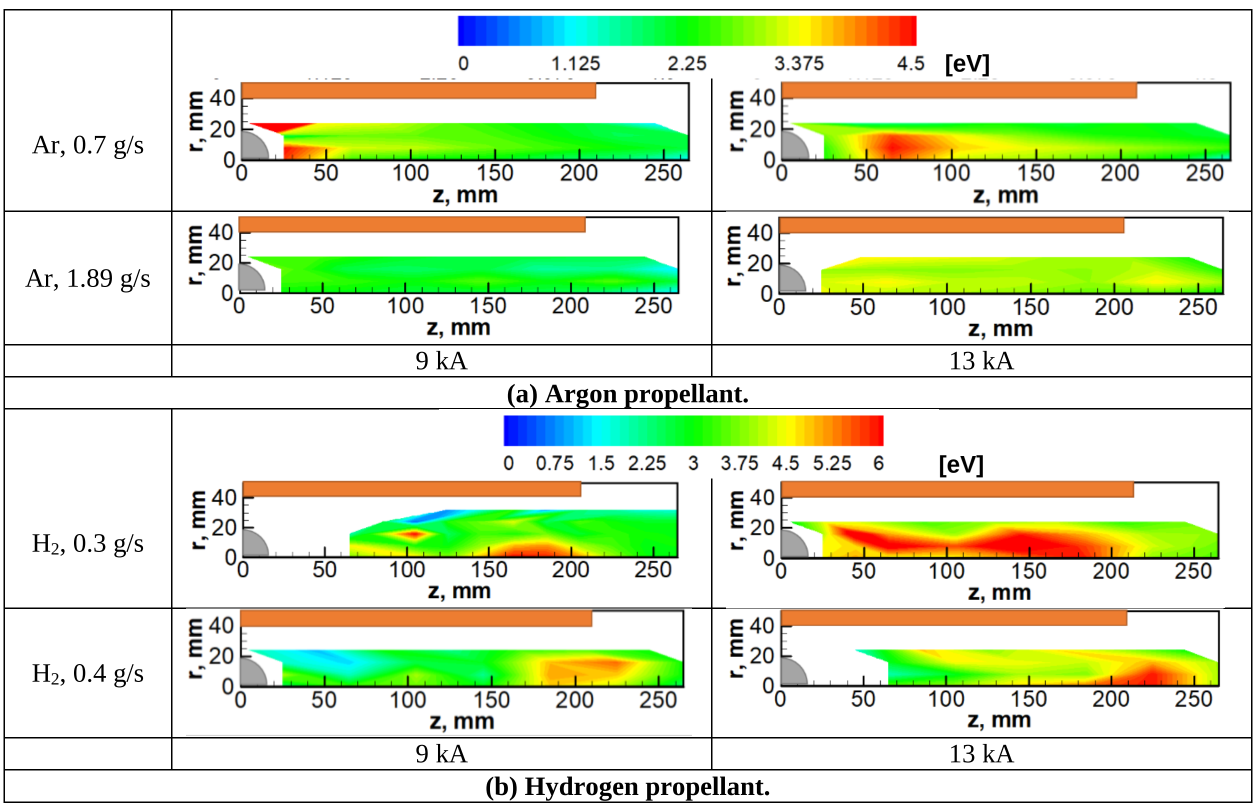

Fig. 11 Electron temperature distributions [eV].

and the electron temperature distributions are shown in Fig. 11. In Fig.12, the floating potential and space potential distributions, which case is hydrogen propellant, mass flow rate of 0.3 g/s, discharge current of 9 kA, are shown.

As shown in Fig. 10, the electron number density distributions tend to increase near the cathode tip region, and the electron number density decreased from upstream to downstream in case of argon propellant. The electron number density reached 3.6×10^{-3} m^{-3} at the point of (z, r) = (25 mm, 0 mm). Although the electron number density tends to be concentrated to near cathode tip, the electron number density in radial direction have a small gradient, especially in case of the mass flow rate of 1.89 g/s and discharge current of 13 kA. The reason for this was the characteristics of monoatomic molecule gas. The propellant gas was ionized at the upstream of the discharge chamber in case of monoatomic molecule gas. Therefore, the electrons concentrated to the cathode tip region in case of argon propellant. In the case of hydrogen propellant, the electron number density has lower value compared with the argon propellant cases because of lower mass flow rate compared with argon propellant. The trend of the electron number density distribution was also different from argon cases. According to Fig. 10, the electrons were concentrated to the near cathode tip at the upstream region, however, the electrons expanded to the entire radial direction at the downstream of the discharge chamber in all cases. The reasons for this were propellant species and current path distribution. The hydrogen is a molecular gas, then the propellant was ionized at the downstream of the discharge chamber. Therefore, the many electrons generate at the downstream of the discharge chamber. In addition, our previous numerical study suggested that the current path was extracted and flows in the downstream of discharge chamber.[23] Therefore, the electrons pinched to the near cathode tip region and center axis direction in case of hydrogen as a propellant.

The high electron temperature occurred at the upstream region, in particular near the cathode region, in case of argon propellant. The electron temperature reached to 4.5 eV at the point of (z, r) = (65 mm, 8 mm) in case of the mass flow rate of 0.7 g/s and discharge current of 13 kA. The reason for this was the ionization location of propellant gas. The argon propellant was ionized at upstream of the discharge chamber. On the other hand, the high electron temperature occurred at the downstream region of the discharge chamber in case of hydrogen propellant. However, the electron temperature of hydrogen cases is larger than that for the argon cases in entire discharge chamber region, and the electron temperature reached to 6.9 eV at the point of (z, r) = (145 mm, 8 mm). The electron temperature is higher for lower mass flow cases with both argon and hydrogen propellants.

C. The Relationships between Cathode Surface Temperature and Plasma Spatial Distribution

In this section discuss the relationships between cathode surface temperature distribution and plasma spatial distribution. Figure 12 shows the magnified figure of Figs. 9 to 11 in cases of argon as a propellant, mass flow rate of 1.89 g/s, discharge current of 9 kA and hydrogen as a propellant, mass flow rate of 0.4 g/s, discharge current of 9 kA.

As shown in Fig. 11, it is considered that the electron number density distribution has an effect on the cathode surface temperature distribution, and the electron temperature distribution has an effect on the value of the cathode temperature. Figures 11 (a) and (c) indicate that the electron number density is larger for the hydrogen propellant because of mass flow rate. In case of argon propellant, the electron number density distribution is distributed with uniformity in the near cathode region. On the other hand, the electron number density is concentrated on the central axis (r = 0 mm) in the near cathode region. Regarding the electron temperature distribution, the electron temperature is distributed with uniformity and the high electron temperature is distributed with the cathode root region in case of argon propellant. The reason for this was current path distribution. In previous numerical work[24] suggested that the current flows from anode to the cathode root in case of argon propellant, because argon was ionized at upstream of the discharge chamber. Therefore, the cathode is heated at the cathode root by Joule heating and plasma distribution effect, and the high electron temperature takes place at the near cathode root region. On the other hand, the high electron temperature is distributed at the near cathode tip region in case of hydrogen propellant. The reason for this was also current path distribution. In our numerical study suggested that the current flows from anode to cathode tip in case of hydrogen propellant, because the hydrogen propellant was ionized through dissociation and the current path was extracted to the downstream of the discharge chamber. Therefore, the high electron number density region and high electron temperature distribution occur at the cathode tip region, and the cathode was heated significantly in case of hydrogen propellant.

In addition, it is considered that the ions have an effect on the cathode surface temperature distribution. The reason for this was plasma spatial distribution in case of hydrogen propellant. As stated before paragraph, the high electron number density region and high electron temperature distribution occur at the cathode tip region in case of hydrogen propellant, and the cathode heated at the cathode tip. In the near cathode tip region, it is expected that the ions are bombarded to the cathode electrode.

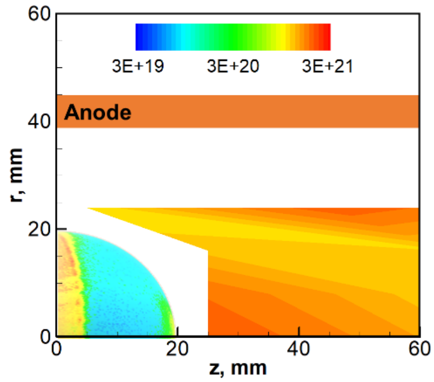

(a) Cathode surface temperature [K] and electron number density [m^{-3}] distribution (Ar, 1.89 g/s).

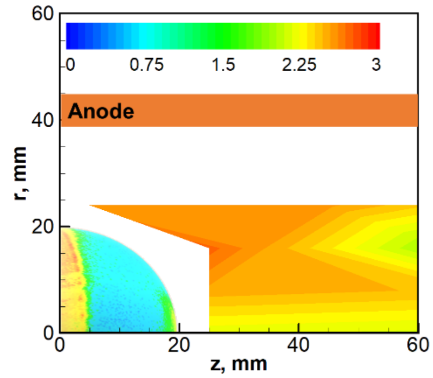

(b) Cathode surface temperature [K] and electron temperature [eV] distribution (Ar, 1.89 g/s).

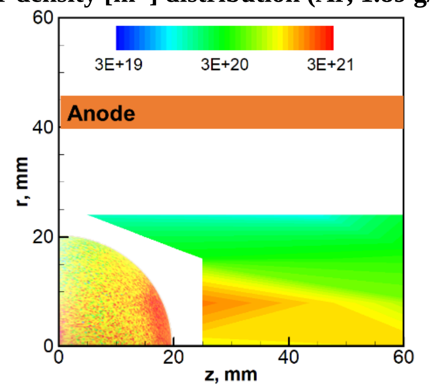

(c) Cathode surface temperature [K] and electron number density [m^{-3}] distribution (H_2, 0.4 g/s).

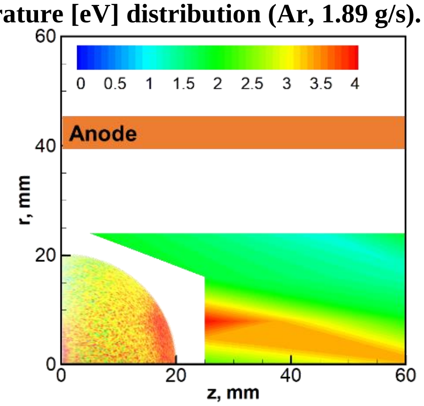

(d) Cathode surface temperature [K] and electron temperature [eV] distribution (H_2, 0.4 g/s).

Fig. 12 Magnified figures of cathode surface temperature and plasma spatial distribution at 9 kA.

IV.Conclusion

To clarify the relationships between cathode surface temperature distribution and plasma spatial distribution, cathode temperature measurement and plasma diagnostics were conducted by using the two-color thermography and double Langmuir probe for the straight anode MPD thruster. The conclusions of this study are shown as follows;

are shown as follows;

1. The cathode mainly heated both cathode tip and root in case of argon as a propellant, however, in case of hydrogen as a propellant, the cathode was mainly heated on the cathode tip
2. The electrons were concentrated to the near cathode tip region with both argon and hydrogen propellant cases. Although the electron number density tends to be concentrated to near cathode tip, the electron number density in radial direction have a small gradient in case of argon propellant. However, the electron number density in radial direction has a large gradient in case of hydrogen propellant because of its extracted current path.
3. As the results, it is considered that the electron number density distribution has an effect on the cathode surface temperature distribution, and the electron temperature distribution has an effect on the value of the cathode temperature.

References

1 Gilland, J. H., "Mission and System Optimization of NEP Vehicles for Lunar and Mars Mission," *Proceedings of the 22nd IEPC*, 1991, p. IEPC-91-038.

2 Percy, T., McGuire, M., and Polsgrove, T., "In-space transportation for NASA's Evolvable Mars Campaign," *AIAA SPACE 2015 Conference and Exposition*, Reston, Virginia: American Institute of Aeronautics and Astronautics, 2015, pp. 1–19.

3 ISECG, *The Global Exploration Roadmap*, 2018.

[4] LaPointe, M., Oleson, S., Pencil, E., Mercer, C., Di Stefano, S., Gilland, J., and Mason, L., "MW-Class Electric Propulsion System Designs for Mars Cargo Transport," *AIAA SPACE 2011 Conference & Exposition*, Reston, Virginia: American Institute of Aeronautics and Astronautics, 2011, pp. 1–15.

[5] Gilland, J., LAPOINTE, M., and Mikellides, P. G., "Megawatt Electromagnetic Plasma Propulsion," *Technology and Systems Options Towards Megawatt Level Electric Propulsion Workshop*, 2003.

[6] Dankanich, J., Vondra, B., and Ilin, A., "Fast Transits to Mars Using Electric Propulsion," *46th AIAA/ASME/SAE/ASEE Joint Propulsion Conference & Exhibit*, Reston, Virginia: American Institute of Aeronautics and Astronautics, 2010, pp. 1–20.

[7] Bérend, N., Moreno, E. C., Ruault, J.-M., and Epenoy, R., "Feasibility Assessment of Rapid Earth-Mars Transfers Using High-Power Electric Propulsion," *Journal of Spacecraft and Rockets*, vol. 51, May 2014, pp. 946–957.

[8] Jahn, R. G., *Physics of Electric Propulsion*, New York: McGraw-Hill, Inc., 1968.

[9] Frisbee, R., "Evaluation of High-Power Solar Electric Propulsion Using Advanced Ion, Hall, MPD, and PIT Thrusters for Lunar and Mars Cargo Missions," *42nd AIAA/ASME/SAE/ASEE Joint Propulsion Conference & Exhibit*, Reston, Virginia: American Institute of Aeronautics and Astronautics, 2006.

[10] Sovey, J. S., and Mantenieks, M. A., "Performance and lifetime assessment of magnetoplasmadynamic arc thruster technology," *Journal of Propulsion and Power*, vol. 7, Jan. 1991, pp. 71–83.

[11] Malliaris, A. C., John, R. R., Garrison, R. L., and Libby, D. R., *Quasi-steady MPD propulsion at high power*, 1971.

[12] Choueiri, E. Y., and Ziemer, J. K., "Quasi-Steady Magnetoplasmadynamic Thruster Performance Database," *Journal of Propulsion and Power*, vol. 17, Sep. 2001, pp. 967–976.

[13] Oshio, Y., Tonooka, S., and Funaki, I., "Thrust Performance and Cathode Temperature Evaluation of MW Class Quasi-Steady MPD Thruster," *52nd AIAA/SAE/ASEE Joint Propulsion Conference*, Reston, Virginia: American Institute of Aeronautics and Astronautics, 2016, p. AIAA 2016-5039.

[14] Tauchi, S., Oshio, Y., Kawasaki, A., Kubota, K., and Funaki, I., "Analysis of Thrust Performance and Cathode Phenomena on a Megawatt-Class MPD Thruster," *AIAA SciTech 2019 Forum*, Reston, Virginia: American Institute of Aeronautics and Astronautics, 2019, pp. 1–12.

[15] Kawasaki, A., Kubota, K., Funaki, I., and Okuno, Y., "MHD and Thermal Coupled Simulation of an MPD Thruster," *51st AIAA/SAE/ASEE Joint Propulsion Conference*, Reston, Virginia: American Institute of Aeronautics and Astronautics, 2015, pp. 1–9.

[16] Sato, H., Kubota, K., and Funaki, I., "Numerical Study of a Hydrogen Plasma Flow Field in a Self-Field Magnetoplasmadynamic Thruster," *42nd AIAA Plasmadynamics and Lasers Conference*, Reston, Virginia: American Institute of Aeronautics and Astronautics, 2011, pp. 1–8.

[17] Tauchi, S., OSHIO, Y., Kawasaki, A., and Funaki, I., "Experimental Study of Quasi-Steady Self-Field MPD Thrusters with Various Cathode Configurations," *Proceedings of 32nd ISTS ISTS*, 2019, pp. 2019-b-043.

[18] Auweter-Kurtz, M., Glocker, B., Kurtz, H. L., Loesener, O., Schrade, H. O., Tubanos, N., Wegmann, T., Willer, D., and Polk, J. E., "Cathode phenomena in plasma thrusters," *Journal of Propulsion and Power*, vol. 9, Nov. 1993, pp. 882–888.

[19] Andrenucci, M., Paganucci, F., and Turco, A., "MPD Thruster Plume Diagnostics," *Proceedings of the 19th IEPC*, 1993, p. IEPC-93-141.

[20] Kagaya, Y., and Yoshikawa, T., "Experimental and theoretical researches on arc structure in a self-field thruster," *19th International Electric Propulsion Conference*, Reston, Virginia: American Institute of Aeronautics and Astronautics, 1987.

[21] Turchi, P. J., and Jahn, R. G., "Cathode Region of a Quasi-Steady MPD Arcjet," *AIAA Journal*, vol. 9, Jul. 1971, pp. 1372–1379.

[22] Lobbia, R. B., and Beal, B. E., "Recommended Practice for Use of Langmuir Probes in Electric Propulsion Testing," *Journal of Propulsion and Power*, vol. 33, May 2017, pp. 566–581.

[23] Tauchi, S., Kawasaki, A., Nakane, M., Kubota, K., and Funaki, I., "The Effect of Anode Configuration on Hydrogen MPD Thruster Performance: A Numerical Study," *TRANSACTIONS OF THE JAPAN SOCIETY FOR AERONAUTICAL AND SPACE SCIENCES, AEROSPACE TECHNOLOGY JAPAN*, vol. 16, 2018, pp. 274–279.

[24] Kubota, K., Funaki, I., and Okuno, Y., "Numerical Study of Plasma Behavior in a Magnetoplasmadynamic Thruster Around Critical Current," *Journal of Propulsion and Power*, vol. 25, Mar. 2009, pp. 397–405.